Check for updates

Nonadiabatic wave packet dynamics and predissociation resonances in sodium hydride

Hans O. Karlsson (ORCID)

Vibrational wave packet dynamics provides an opportunity to explore the energy landscape and the population transfer between nonadiabatically coupled excited electronic states. Here the coupled nonadiabatic dynamics of the $C^1\Sigma^+$ and $D^1\Sigma^+$ states of sodium hydride (NaH) in the gas phase in the adiabatic picture is studied, using a sequence of ultra-fast laser pulses in the femtosecond region. Emergence of different population dynamics and dissociation probabilities is shown by carefully choosing the pulse wavelength, duration and time-shift between the pulses, exciting the molecule from the ground $X^1\Sigma^+$ state *via* the immediate $A^1\Sigma^+$ state. Quantum dynamics simulations were performed in the adiabatic picture, avoiding the adiabatic to diabatic transformation. Predissociation resonances, *i.e.* vibrational states with finite lifetimes, arise due to nonadiabatic couplings between bound and continuum states. Here accurate resonance energies and widths are computed providing further insight into the dissociation dynamics.

1 Introduction

With the advent of femtochemistry in the late 1980s it became possible to study chemical reactions in real time, following the breaking and making of chemical bonds as well as clocking the transition state.[1,2] Laser pulses in the femtosecond region provide a balance in resolution for the nuclear dynamics between the time and energy domains. The field of femtochemistry opened up the possibility to study molecular dynamics far from the equilibrium region, necessitating the inclusion of nonadiabatic couplings between electronic states in the simulations, due to the break-down of the Born–Oppenheimer approximation.[1] Furthermore, nonadiabatic couplings between bound and continuum energies on different electronic states give rise to predissociation resonances, *i.e.* vibrational states with finite lifetimes.[3] Faster pulses, *e.g.* in the attosecond regime, provide a high temporal resolution but with a broad energy distribution. In the other extreme very long laser pulses, *e.g.* in the nanosecond regime, lead to a high resolution in energy but with a low temporal resolution.

Femtosecond laser pulses give rise to a coherent superposition of vibrational states, *i.e.* vibrational wave packets.[2] By combining several ultrafast pulses, with different wavelengths λ, pulse durations τ and time shifts T between the pulses, different regions of the potential energy landscape, as well as population transfer between electronic states, can be investigated and analyzed.[1] The potential energy surfaces (PESs) and

Division of Scientific Computing, Department of Information Technology, Box 337, SE-751 05, Uppsala, Sweden. E-mail: Hans.Karlsson@it.uu.se

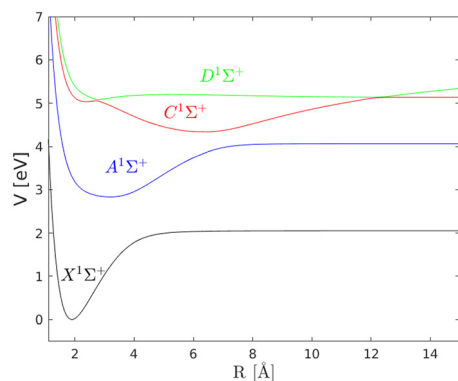nonadiabatic couplings are computed in the adiabatic formalism using quantum chemical methodology, whereas the wave packet simulations of the nuclear dynamics normally are performed in the diabatic representation, necessitating an adiabatic to diabatic transformation.[4] In a recent study Talbot *et al.*[5] computed the accurate PES and nonadiabatic couplings for the sodium hydride (NaH) molecule. The potential energy surfaces and first-order derivative couplings were computed using equation-of-motion coupled cluster theory with single and double excitations (EOM-EE-CCSD), with core-valence polarized basis functions. In the region around 12 Å issues with the convergence of the surfaces and couplings were noted, as can be observed in the reported C and D states close to the second avoided crossing. Using the sudden approximation, vibrational wave packet dynamics on the excited electronic $|A\rangle$, $|C\rangle$ and $|D\rangle$ states were studied, using both quantum and semi-classical methods. Their simulations illustrated that the adiabatic picture can be used for the quantum and semi-classical simulations, avoiding the need for an adiabatic to diabatic transformation.

In this work the adiabatic picture is used to compute accurate predissociation resonances and quantum wave packet dynamics explicitly initiated by a sequence of femtosecond laser pulses, using the potentials, Fig. (1), and nonadiabatic couplings, Fig. (2), computed by Talbot *et al.*[5] Similar potential energy surfaces for NaH, although no derivative couplings, were also computed by Aymar *et al.*[6]

The ground electronic state $|X\rangle$ of NaH has an equilibrium distance of $R_{eq}^X = 1.87$ Å, whereas the minimum of the first excited state $|A\rangle$ is located at $R_{eq}^A = 3.19$ Å. Following an

8482 | *Phys. Chem. Chem. Phys.*, 2023, **25**, 8482–8488

This journal is © the Owner Societies 2023

Fig. 1 Potential energy surfaces of sodium hydride relevant for this work. From the study of Talbot *et al.*[5]
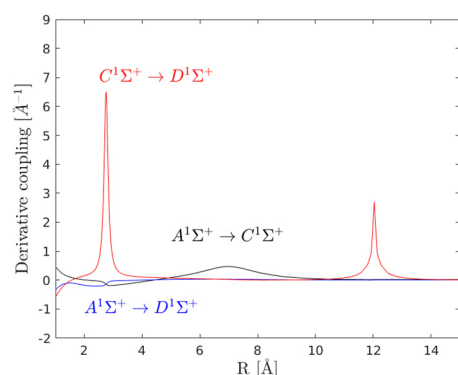

Fig. 2 Nonadiabatic couplings between the A, C and D electronic states. From the study of Talbot *et al.*[5]

excitation from the $|X\rangle$ state to the $|A\rangle$ state, a coherent wave packet will be formed composed of highly excited vibrational states, due to the shift in the equilibrium distance. The $|C\rangle$ electronic state has a local minimum at $R_1^C = 2.38$ Å, and a global minimum at $R_2^C = 6.5$ Å. For the $|D\rangle$ state, there is a minimum at $R_1^D = 2.72$ Å, supporting two vibrational states, and another minima at $R_2^D = 12$ Å. There are two avoided crossings between the $|C\rangle$ and $|D\rangle$ states. The first avoided crossing is located at $R_{c1} = 2.72$ Å, whereas the second avoided crossing is close to $R_{c2} = 12$ Å. Due to the different shapes and anharmonicities of the electronic states, the resulting wave packets will move with different time scales, as will be discussed below.

2 Methods

The vibronic Schrödinger equation was discretized on a grid, with a grid spacing of d$R = 0.015$ Å, using pseudo-spectral/ sincDVR[7–9] and high order finite difference[10] methods. Different grid sizes, ranging from 15 Å up to 40 Å, were used to describe the wave packet dynamics and resonance states. The

Hamiltonian, including nonadiabatic and time-dependent couplings, is given by[5,11]

$$\hat{H} = \frac{1}{2\mu}\left(\hat{P} - i\hbar\hat{d}(R)\right)^2 + V(R) + V^t(t) \tag{1}$$

where μ is the reduced mass, $\hat{P} = -i\hbar\nabla_R$ is the momentum operator and $\hat{d}$ is the skew-symmetric matrix of first order derivative coupling vectors. The transition dipole moment is assumed to be constant and the time-dependent term $V^t(t)$ describes the interaction with an ultrafast laser pulse in the dipole approximation.

3 Predissociation resonances

The nonadiabatic coupling between the $|C\rangle$ and $|D\rangle$ electronic states leads to a bound-continuum coupling giving rise to predissociation resonances *i.e.* vibrational states with a finite lifetime. The nonadiabatic coupling between the $|A\rangle$ and the $|C\rangle$ and $|D\rangle$ states, respectively, also contributes to the resonance structure but with a minor effect on the resonance lifetime due to the weaker coupling strength. Earlier studies on the predissociation of the NaH molecule include radiative and predissociative decay from the A state for high rotational numbers.[12] Here, the focus is on the vibrational predissociation for the coupled C and D states.

The predissociation resonances are represented as complex valued energies $E = E_r - iE_i$, where the real part E_r gives the position of the energy and the negative imaginary part is related to the width of the resonance $E_i = \Gamma/2$, which in turn is related to the lifetime of the resonance $\tau_{res} = \hbar/\Gamma$.[3,13,14] To determine the resonance states, the time-independent vibronic Schrödinger equation

$$\hat{H}|\Phi\rangle = E|\Phi\rangle \tag{2}$$

was solved using the vibronic Hamiltonian (1) without the time-dependent coupling term. Numerical tools based on smooth exterior scaling (SES)[13,15] and the closely related perfectly matching layer (PML)[10] method were used to compute the predissociation resonances. The main difference between the SES and PML methods is that in the PML approach the potentials are not scaled and the scaling is performed after the grid discretization. From the theory of complex scaling,[13] it is known that bound states and resonances are independent of the scaling parameters whereas the continuum states will rotate down in the complex plane, exposing the resonances. For a discretized Schrödinger equation, there will be a minor parameter dependence of the bound states and resonances, giving rise to a small trajectory in the complex plane. The continuum states will have a major dependence on the scaling parameters, with a large movement in the complex plane, and thus, it is straightforward to distinguish the bound states and resonances from the continuum states. Smooth exterior scaling is implemented by scaling the coordinate $R \rightarrow F(R)$ such that the region $R < R_0$ remains unaffected by transformation and with a small damping region $R \geq R_0$. Here, $f(R) = \dfrac{dF(R)}{dR} = 1 + (e^{i\theta} - 1)g(R)$ where θ is the scaling angle and $g(R)$ is a

This journal is © the Owner Societies 2023

Phys. Chem. Chem. Phys., 2023, **25**, 8482–8488 | **8483**

smooth function that changes from 0 to 1 around $R = R_0$.[13,15] The switching function $g(R)$ can be of a general form as long as it is smooth; here, the shape proposed by Moiseyev[13] was used. When solving for the time-independent Schrödinger equation using SES or PML, the same discretization for the kinetic energy operator $\hat{T} = \dfrac{\hat{P}^2}{2\mu}$ for bound states can be used, modified by pre- and post-multiplication with the inverse of $f(R)$ and adding a small potential term $V_{SES}(R)$,

$$\hat{T}_{SES} = f^{-1}\hat{T}f^{-1} + V_{SES} \tag{3}$$

$$V_{SES} = \frac{1}{8\mu}(2f''f - 3[f']^2)/f^4, \tag{4}$$

which is straightforwardly implemented in the existing computational codes for vibrational eigenstates.[14] Furthermore, if the PES is constant for $R \geq R_0$, it is not affected by the scaling and remains real and constant. Absorbing potentials,[16] where the PES is augmented with a complex damping term $W(R)$ for $R \geq R_0$, i.e. $V(R) \rightarrow V(R) - iW(R)$, provide an alternative approach, having its main strength as an absorber for outgoing wave packets in time-dependent computations.

Fig. (3) displays the predissociation resonance energies and widths for the coupled $|C\rangle$ and $|D\rangle$ electronic states in relation to the respective potential energy surfaces. A close up of the $|C\rangle$ and $|D\rangle$ state resonances is given in Fig. (4). The oscillatory pattern of the resonance widths is a signature of predissociation resonances.[14] For a correct description of the coupled $|C\rangle$ and $|D\rangle$ states, the widths, i.e. lifetimes, of the vibrational resonances must be considered.

The nine highest excited vibrational resonances on the $|C\rangle$ state and the first six resonances on the $|D\rangle$ state are given in Table (1) for comparison with a previous work.[5] The resonance positions compare well with the vibrational energies previously reported except for the D, 2 state which in this work is found to not be degenerate with the D, 3 state, having a slightly lower value of the energy and with a rather large width, i.e. a short
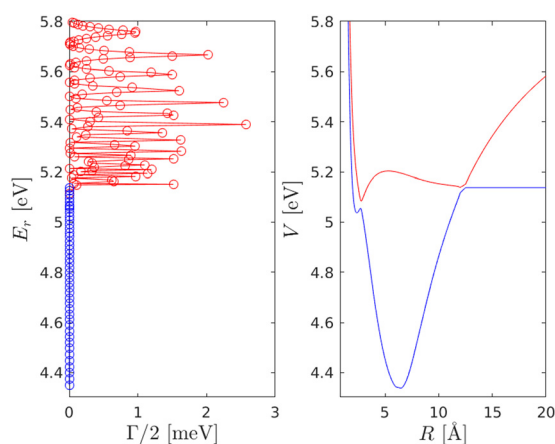

Fig. 3 Predissociation resonances for the $|C\rangle$ and $|D\rangle$ electronic states in relation to the potential energy surfaces. Note that the calculation of the resonances utilized an extended grid up to 40 Å but that for clarity the PES is truncated at 20 Å and 5.8 eV.
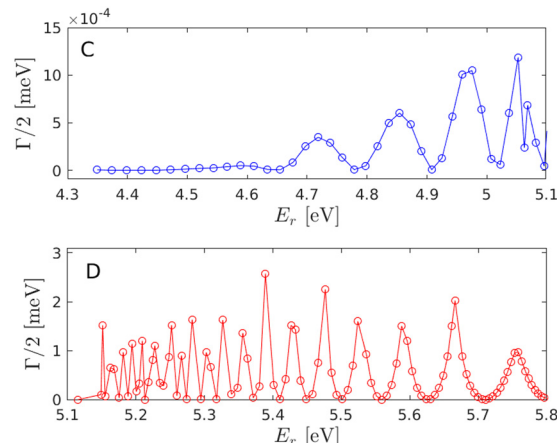

Fig. 4 Predissociation resonances for the $|C\rangle$ and $|D\rangle$ electronic states. Note the different scales for the widths. For clarity, the same energy range is used as shown in Fig. (3).

Table 1 Positions E_r and widths $\Gamma/2$ for the selected predissociation resonances of the $|C\rangle$ and $|D\rangle$ electronic states

State	Previous work[5] E_r (eV)	This work E_r (eV)	$\Gamma/2$ (meV)
$C^1\Sigma^+$			
34	5.038	5.037	6.0×10^{-7}
35	5.053	5.052	1.2×10^{-6}
36	5.063	5.063	2.4×10^{-7}
37	5.069	5.068	6.9×10^{-7}
38	5.082	5.082	2.9×10^{-7}
39	5.096	5.096	4.4×10^{-8}
40	5.109	5.109	1.1×10^{-6}
41	5.125	5.125	1.6×10^{-6}
42	5.136	5.136	2.1×10^{-6}
$D^1\Sigma^+$			
0	5.116	5.115	9.9×10^{-8}
1	5.149	5.149	1.0×10^{-4}
2	5.155	5.151	1.5×10^{-3}
3	5.155	5.155	7.1×10^{-5}
4	5.162	5.162	6.5×10^{-4}
5	5.169	5.168	6.2×10^{-4}

lifetime, compared to the neighboring resonances. Note that the nonadiabatic coupling between the $|A\rangle$ and $|C\rangle$ electronic states also give rise to finite lifetimes also for the $|C\rangle$ vibrational states close to the dissociation limit, although with less widths than that for the $|D\rangle$ resonances due to the weaker coupling strength.

4 Wave packet dynamics

Vibrational wave packet dynamics provides a way to explore the energy landscape on the excited electronic states and the effects of the nonadiabatic couplings.[1,2] By using a sequence of ultrafast laser pulses to initiate the wave packet dynamics, different regions of the potential surfaces can be explored and analyzed, e.g. with respect to population transfer, quantum interference and dissociation probabilities. Here, a two pulse, pump–probe type, scheme is used where the first pulse promotes the

8484 | Phys. Chem. Chem. Phys., 2023, **25**, 8482–8488

This journal is © the Owner Societies 2023

probability density from the ground $|X\rangle$ state to the excited $|A\rangle$ electronic state and the second pulse promotes the wave packet from the $|A\rangle$ to the coupled $|C\rangle$ and $|D\rangle$ states. The probability of dissociation from the $|C\rangle$ state depends on the laser pulse but also on the nonadiabatic coupling. The laser pulse is given by

$$V^t(t, t_0) = E_0 e^{-(t-t_0)^2/\alpha^2} \cos(\omega t) \quad (5)$$

$$\alpha = \tau/2\sqrt{\ln 2} \quad (6)$$

assuming the dipole approximation and a Gaussian pulse shape. The strength is given by E_0, the FWHM width of the pulse by τ and t_0 gives the center of the pulse. The wavelength λ enters *via* $\lambda = 2\pi c/\omega$, where c is the speed of light. The two laser pulses will be shifted in time by a time shift T, such that $V^t(t) = V_{\text{pump}}(t, 0) + V_{\text{probe}}(t, T)$. The explicit time-dependent Schrödinger equation

$$i\hbar \frac{\partial |\Psi(t)\rangle}{\partial t} = \hat{H}(t)|\Psi(t)\rangle \quad (7)$$

was solved using the short iterative Arnoldi method[17,18] with the adiabatic Hamiltonian (1) and a second-order Magnus expansion for the time-dependent coupling.[19] A time step of $\mathrm{d}t = 0.05$ fs was used.

4.1 Wave packet dynamics on the electronic $|A\rangle$ state

The ultrafast pump pulse $V_{\text{pump}}(t)$ gives rise to a coherent vibrational wave packet $|\Psi^A(t)\rangle$ by excitation from the ground vibrational state $|\phi_0^X\rangle$. The resulting wave packet $|\Psi^A(t)\rangle$ and its subsequent dynamics depend on the shape of the potential energy surface and the characteristics of the laser pulse, *i.e.* the wavelength λ, pulse duration τ and strength E_0. Here, the strength of the pulse was chosen to be weak, *i.e.* around 98% of the population will remain in the electronic ground state after excitation.

To determine the maximum population transfer from the $|X\rangle$ state to the $|A\rangle$ state, the population on the $|A\rangle$ state was computed as a function of wavelength, using a pump pulse with a duration of $\tau_{\text{pump}} = 10$ fs. As seen in Fig. (5), a maximum
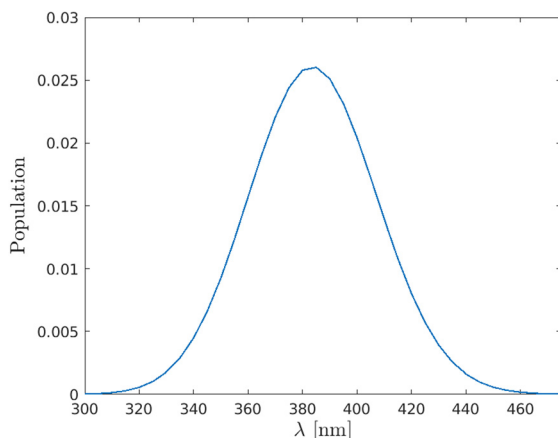
population transfer is observed at $\lambda = 383$ nm, as noted previously.[20–22]

Having established an optimal wavelength for excitation, the effect of the pulse duration τ on the formation of the $|\Psi^A(t)\rangle$ wave packet is considered. Four different pulse lengths were used, ranging from very short ($\tau = 1$ fs), *via* medium length ($\tau = 10$ fs) to very long ($\tau = 25$ fs and $\tau = 50$ fs) in relation to the vibrational period of the $|A\rangle$ state. The resulting wave packet dynamics up to 200 fs as a function of pulse duration τ is shown in Fig. (6).

To understand the time-evolution of the wave packet $|\Psi^A(t)\rangle$, a decomposition in terms of vibrational eigenstates can be used for illustration

$$|\Psi^A(t)\rangle\rangle = \sum_n c_n |\phi_n^A\rangle e^{-iE_n^A t/\hbar} \quad (8)$$

For the pump pulse used here only bound vibrational states $|\phi_n^A\rangle$ will contribute to the wave packet. The coefficients c_n in the superposition (8) contain the overlap between the nuclear vibrational eigenfunctions $|\phi_n^A\rangle$ and the ground vibrational state $|\phi_0^X\rangle$, as in the sudden approximation formalism, but also the effect of the ultrafast laser pulse *i.e.* the wavelength and pulse duration. Integrated over the duration of the pulse, the coefficients c_n can be expressed as[23]

$$c_n = \mu_0 \langle \phi_n^A | \phi_0^X \rangle f(\omega, \lambda) \quad (9)$$

$$f(\omega, \lambda) = E_0 e^{-\alpha^2(\omega-\omega_{n0})^2/4} \quad (10)$$

$$\alpha = \tau/2\sqrt{\ln 2} \quad (11)$$

$$\omega_{n0} = (E_n^A - E_0^X)/\hbar \quad (12)$$

assuming a constant dipole moment μ_0. In Fig. (7), the absolute values of the coefficients $|c_n|^2$ are shown for the four cases
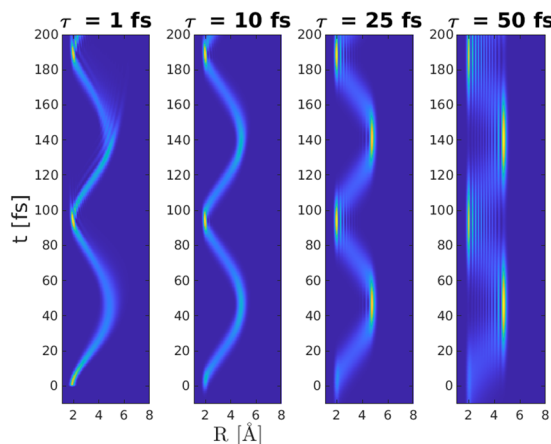
Fig. 5 Population on the $|A\rangle$ state as a function of the pump wavelength, using a pulse duration of $\tau = 10$ fs.

Fig. 6 Wave packet dynamics on the $|A\rangle$ state as a function of pulse duration τ, using a wavelength of $\lambda = 383$ nm. It is noticed that the shape of the wave packet depends on the pulse duration whereas the revival time is similar $T_{\text{ref}} = 95$ fs. It is further noticed that the population on the $|A\rangle$ state differ for the four different situations, as shown in Fig. (7).
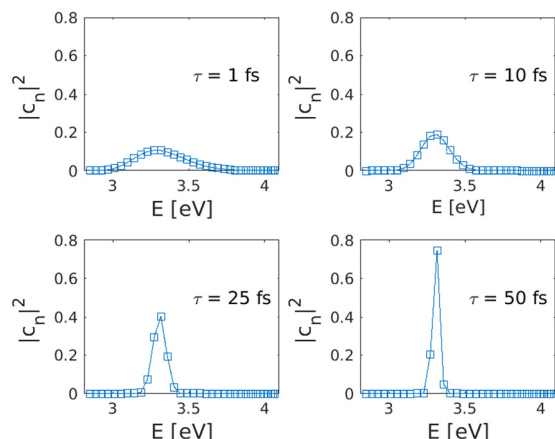
This journal is © the Owner Societies 2023

Phys. Chem. Chem. Phys., 2023, **25**, 8482–8488 | **8485**

Fig. 7 Probability $|c_n|^2$, eqn (9), for the molecule to be in the vibrational state $|\phi_n^A\rangle$ as a function of vibrational energy for four different pulse durations, $\tau = 1$ fs, $\tau = 10$ fs, $\tau = 25$ fs and $\tau = 50$ fs.

studied here. The excitation leads to wave packets that are centered on the 11:th excited vibrational state, $E_{11} = 3.3$ eV.

For a short pulse duration, $\tau = 1$ fs, the coefficients c_n are close to the Frank–Condon factors, which correlate with the sudden approximation where it is assumed that the wave packet do not move during the excitation process and the resulting weights in the wave packet are given by the overlap of the vibrational states with the initial ground vibrational state $c_n = \langle\phi_n^A|\phi_0^X\rangle$. In the other extreme, $\tau = 50$ fs, corresponding to a half vibrational period, the wave packet is dominated by a single vibrational state, in a Golden Rule type of description with an energy matching between the initial and the final states. For the excitation considered here, a duration of $\tau = 10$ fs provides a balance between time and energy resolution. Consequently, in what follows, a pump wavelength of $\lambda_{\text{pump}} = 383$ nm and a duration of $\tau_{\text{pump}} = 10$ fs will be used. To support the discussion in the following section, the resulting wave packet on the $|A\rangle$ state is depicted in Fig. (8).

4.2 Nonadiabatic wave packet dynamics on the $|C\rangle$ and $|D\rangle$ electronic states

The wave packet dynamics on the coupled $|C\rangle$ and $|D\rangle$ electronic states is initiated with a second pulse $V_{\text{probe}}(t + T)$, promoting the probability density from the $|A\rangle$ state. Due to the nonadiabatic couplings, the wave packet can dissociate on the $|C\rangle$ state either directly or *via* the bound $|D\rangle$ state due to the nonadiabatic coupling, as illustrated by the predissociation resonances in the previous section. The resulting wave packet dynamics depends not only on the probe wavelength λ_{probe} and pulse duration τ_{probe} but also on the time shift T between the two pulses, since the $|\Psi^A(t)\rangle$ wave packet will move on the potential energy surface during the probe process. Fig. (9) depicts the population on the $|C\rangle$ and $|D\rangle$ states as a function of wavelength λ_{probe} and time shift T directly after the probe pulse is over. From Fig. (9), it is seen that there are combinations of wavelengths λ and time shifts T where the population on the two states differs significantly. By carefully choosing the probe pulse parameters, the formation of the wave packet on the coupled states can be controlled. As the wave packet evolves in time, different regions of the coupled PES are explored with a probability of population transfer between the coupled states and for dissociation. When the wave packet is close to the crossing regions at $R_{c1} = 2.72$ Å and $R_{c2} = 12$ Å, part of the wave packet might be transferred between the bound $|D\rangle$ state and the unbound part of the $|C\rangle$ state, and dissociate to the Na(4s) + H(1s) limit.

Four different situations were studied to showcase the effect on the dynamics and dissociation probabilities due to different wavelengths λ_{probe} and time shifts T, as well as the importance of the nonadiabatic couplings. The four cases were as follows:

(a) $\lambda_{\text{probe}} = 550$ nm and $T = 14$ fs, corresponding to the wave packet $|\Psi^A(t)\rangle$ being close to the first crossing region between the $|C\rangle$ and $|D\rangle$ states at the probe time T, *i.e.* $\langle\hat{R}\rangle = \langle\Psi^A(T)|\hat{R}|\Psi^A(T)\rangle = 2.8$ Å, and moving outwards, Fig.(10).

(b) $\lambda_{\text{probe}} = 650$ nm and $T = 47$ fs, when $|\Psi^A(t)\rangle$ is at the outer turning point, $\langle\hat{R}\rangle = 5$ Å, Fig. (11).
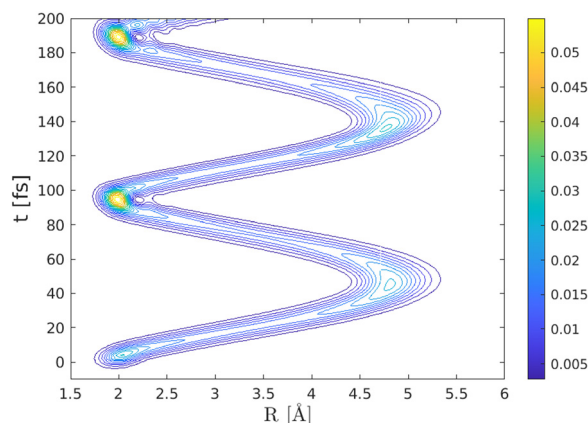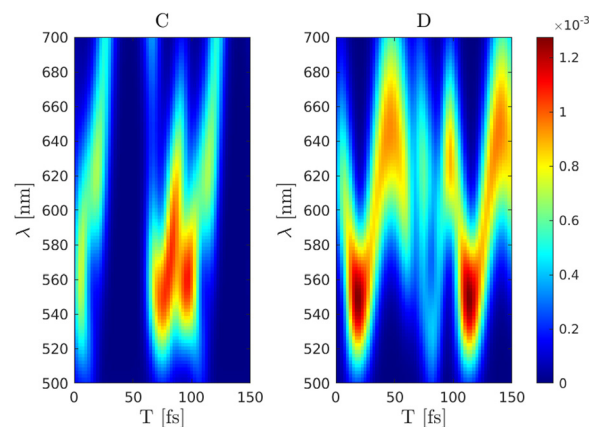

Fig. 8 Probability density of the time-evolution on the A-state after a pump pulse with $\lambda_{\text{pump}} = 383$ nm and $\tau_{\text{pump}} = 10$ fs.

Fig. 9 Population on the $|C\rangle$ and $|D\rangle$ states after excitation from the $|A\rangle$ state as a function of wavelength λ and time shift T with a pulse duration of $\tau = 10$ fs, from low (blue) to high (red) probability.

8486 | *Phys. Chem. Chem. Phys.*, 2023, **25**, 8482–8488

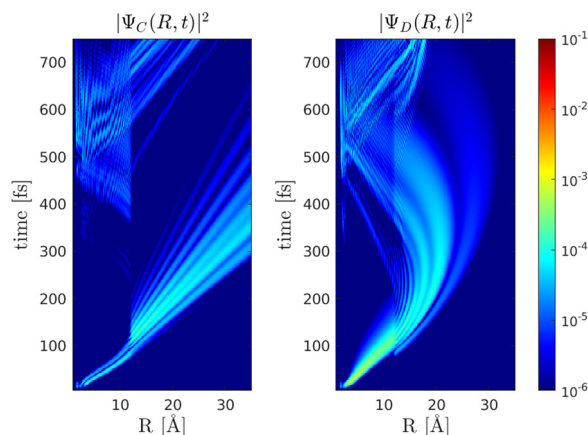This journal is © the Owner Societies 2023

Fig. 10 Probability densities for the dynamics of the $|\Psi^C(t)\rangle$ and $|\Psi^D(t)\rangle$ wave packets for a probe pulse with τ = 10 fs and λ_{probe} = 550 nm at T = 14 fs. At the center of the pulse, $\langle \hat{R} \rangle = \langle \Psi^A(T)|\hat{R}|\Psi^A(T)\rangle$ = 2.8 Å. The population transfer at the outer crossing point R_{c2} = 12 Å is noticed.
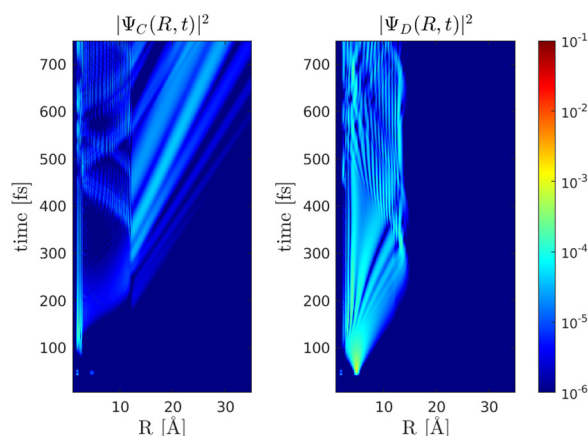

Fig. 12 Probability densities for the dynamics of the $|\Psi^C(t)\rangle$ and $|\Psi^D(t)\rangle$ wave packets for a probe pulse with τ = 10 fs and λ_{probe} = 550 nm at T = 82 fs. At the center of the pulse $\langle \hat{R} \rangle = \langle \Psi^A(T)|\hat{R}|\Psi^A(T)\rangle$ = 2.8 Å.
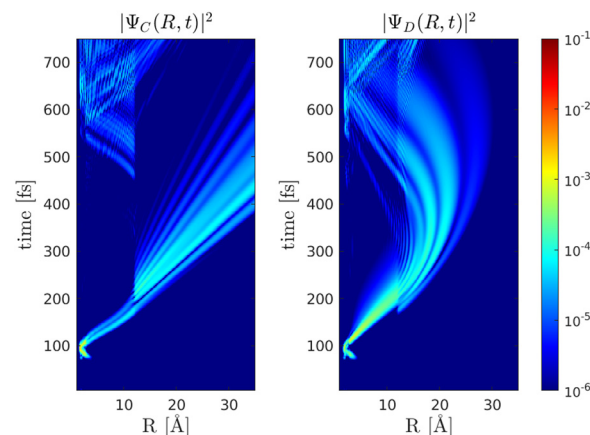

Fig. 11 Probability densities for the dynamics of the $|\Psi^C(t)\rangle$ and $|\Psi^D(t)\rangle$ wave packets for a probe pulse with τ = 10 fs and λ_{probe} = 650 nm at T = 47 fs. At the center of the pulse $\langle \hat{R} \rangle = \langle \Psi^A(T)|\hat{R}|\Psi^A(T)\rangle$ = 5 Å.
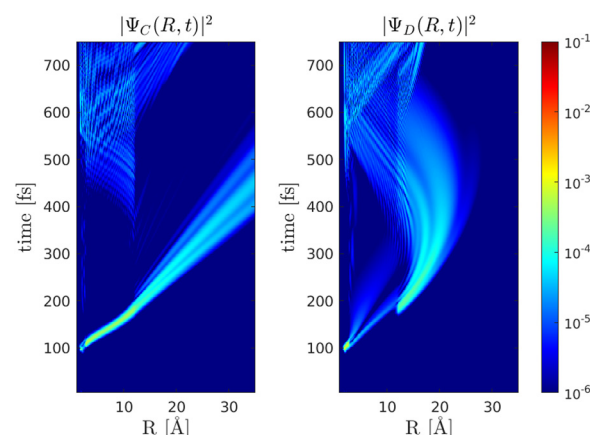

Fig. 13 Probability densities for the dynamics of the $|\Psi^C(t)\rangle$ and $|\Psi^D(t)\rangle$ wave packets for a probe pulse with τ = 10 fs and λ_{probe} = 550 nm at T = 95 fs. At the center of the pulse, $\langle \hat{R} \rangle = \langle \Psi^A(T)|\hat{R}|\Psi^A(T)\rangle$ = 1.8 Å.

(c) λ_{probe} = 550 nm and T = 82 fs, when $|\Psi^A(t)\rangle$ is close to $\langle \hat{R} \rangle$ = 2.8 Å moving inwards, Fig. (12), and

(d) λ_{probe} = 550 nm and T = 95 fs when $|\Psi^A(t)\rangle$ is at the inner turning point, $\langle \hat{R} \rangle$ = 1.8 Å, Fig. (13).

The $|\Psi^D(t)\rangle$ wave packet has a revival period of $T_{\text{rev}} \sim 500$ fs, compared to $T_{\text{rev}} \sim 95$ fs for the $|\Psi^A(t)\rangle$ wave packet. Furthermore, the dynamics of $|\Psi^A(t)\rangle$ is limited to a region in space that is less than $R = 5.5$ Å, whereas the motion of $|\Psi^D(t)\rangle$ extends beyond 25 Å. For case (a), Fig. (10), the excitation energy is above the dissociation limit for the $|C\rangle$ state and the wave packet $|\Psi^C(t)\rangle$ starts to dissociate. As the outgoing wave packet $|\Psi^D(t)\rangle$ passes the outer crossing point R_2^C = 12 Å, the population is transferred to the $|C\rangle$ state, increasing the dissociation probability. A second crossing due to the inwards motion further transfer population, leading to a $|\Psi^C(t)\rangle$ wave packet being reflected at the inner turning point before dissociating. The second combination, (b), Fig. (11), creates wave packets

close to the inner crossing region R_{c1} = 2.72 Å with a mix of bound and dissociative dynamics. The initial excitation is close to 5 Å after which the wave packet quickly spreads towards both the inner and outer turning points. A partially bound state wave packet $|\Psi^C(t)\rangle$ is formed on the $|C\rangle$ state and each time $|\Psi^D(t)\rangle$ passes the outer crossing point there is a probability transfer supporting both inward and outward motions on the $|C\rangle$ state.

The parameters used in case (c), Fig. (12), where $|\Psi^A(t)\rangle$ moves inwards, leads to a similar population probability for the two states, one dissociative $|\Psi^C(t)\rangle$ and one bound $|\Psi^D(t)\rangle$ wave packet. The effect on the nonadiabatic coupling is clearly seen around t = 200 fs and again from $t > 500$ fs. The similarity to case (a) is noticed, and the excitation is taking place on a similar part of the PES but for outward (a) and inward (c) motions, respectively.

For the fourth example (d), Fig. (13), the pulse parameters are chosen such that the population on the $|C\rangle$ state initially dominates, leading to a dissociative wave packet. As $|\Psi^C(t)\rangle$ reaches the outer crossing point a population transfer occurs

This journal is © the Owner Societies 2023

Phys. Chem. Chem. Phys., 2023, **25**, 8482–8488 | **8487**

and a wave packet $|\Psi^D(t)\rangle$ is formed which, in turn, transfer the probability back to the $|C\rangle$ state from $t > 450$ fs.

From these four examples, it is seen that a very rich, both bound and dissociative, nonadiabatic wave packet dynamics can be observed depending on the nonadiabatic couplings and the choice of the pulse parameters.

5 Conclusions

In this work accurate wave packet dynamics, in the adiabatic picture, were computed for the coupled $C^1\Sigma^+$ and $D^1\Sigma^+$ states initiated by a sequence of femtosecond laser pulses. It was illustrated that the wave packet dynamics and population transfer crucially depend on the different combinations of wavelengths, durations and time-shifts between the pulses. Predissociation resonances, emerging due to the coupling between bound and continuum states, provide a complementary illustration of the nonadiabatically coupled system and showing the importance of computing resonance widths.

Further studies will consider the use of optimal control for defining optimal pulse parameters to control different dissociation pathways.

Conflicts of interest

There are no conflicts to declare.

References

1 A. Zewail, *Science*, 1988, **242**, 1645–1653.
2 J. Polanyi and A. Zewail, *Acc. Chem. Res.*, 1995, **28**, 119–132.
3 N. Moiseyev, P. Certain and F. Weinhold, *Mol. Phys.*, 1978, **36**, 1613–1630.
4 W. Domcke and D. R. Yarkony, in *Annual Review of Physical Chemistry*, ed. M. A. Johnson and T. J. Martinez, Annual Reviews, Palo Alto, 2012, vol. 63, pp. 325–352.
5 J. J. Talbot, M. Head-Gordon, W. H. Miller and S. J. Cotton, *Phys. Chem. Chem. Phys.*, 2022, **24**, 4820–4831.
6 M. Aymar, J. Deiglmayr and O. Dulieu, *Can. J. Phys.*, 2009, **87**, 543–556.
7 C. Schwartz, *J. Math. Phys.*, 1985, **26**, 411–415.
8 D. Colbert and W. Miller, *J. Chem. Phys.*, 1992, **96**, 1982–1991.
9 B. Fornberg, *A Practical Guide to Pseusdospectral Methods*, Cambridge University Press, Cambridge, 1996.
10 A. Nissen, H. O. Karlsson and G. Kreiss, *J. Chem. Phys.*, 2010, **133**, 054306.
11 W. Domcke, D. Yarkony and H. Köppel, *Conical intersections: electronic structure, dynamics spectroscopy*, World Scientific, Singapore, 2004.
12 H. Telle, *J. Mol. Struct.*, 1986, **143**, 565–568.
13 N. Moiseyev, *Phys. Rep.*, 1998, **302**, 212–293.
14 H. O. Karlsson, *Eur. Phys. J. D*, 2000, **11**, 207–212.
15 H. O. Karlsson, *J. Chem. Phys.*, 1998, **108**, 3849–3853.
16 R. Kosloff and D. Kosloff, *J. Comput. Phys.*, 1986, **63**, 363–376.
17 T. Park and J. Light, *J. Chem. Phys.*, 1986, **85**, 5870–5876.
18 W. T. Pollard and R. A. Friesner, *J. Chem. Phys.*, 1994, **100**, 5054–5065.
19 K. Kormann, S. Holmgren and H. O. Karlsson, *J. Chem. Phys.*, 2008, **128**, 184101.
20 H.-Y. Huang, Y.-Y. Chang, M.-H. Liao, K.-L. Wu, T.-L. Lu, Y.-Y. Chang, C.-C. Tsai and T.-J. Whang, *Chem. Phys. Lett.*, 2010, **493**, 53–56.
21 H.-Y. Huang, T.-L. Lu, T.-J. Whang, Y.-Y. Chang and C.-C. Tsai, *J. Chem. Phys.*, 2010, **133**, 044301.
22 C.-C. Chu, H.-Y. Huang, T.-J. Whang and C.-C. Tsai, *J. Chem. Phys.*, 2018, **148**, 114301.
23 R. Schinke, *Photodissociation dynamics*, Cambridge University Press, Cambridge, 1993.

8488 | *Phys. Chem. Chem. Phys.*, 2023, **25**, 8482–8488

This journal is © the Owner Societies 2023